Tsunami Modeling to Validate Slip Models of the 2007 M $_w$ 8.0 Pisco Earthquake, Central Peru

M. Ioualalen, H. Perfettini, S. Yauri Condo, C. Jimenez & H. Tavera

Pure and Applied Geophysics
pageoph

ISSN 0033-4553
Volume 170
Number 3

Pure Appl. Geophys. (2013) 170:433-451
DOI 10.1007/s00024-012-0608-z

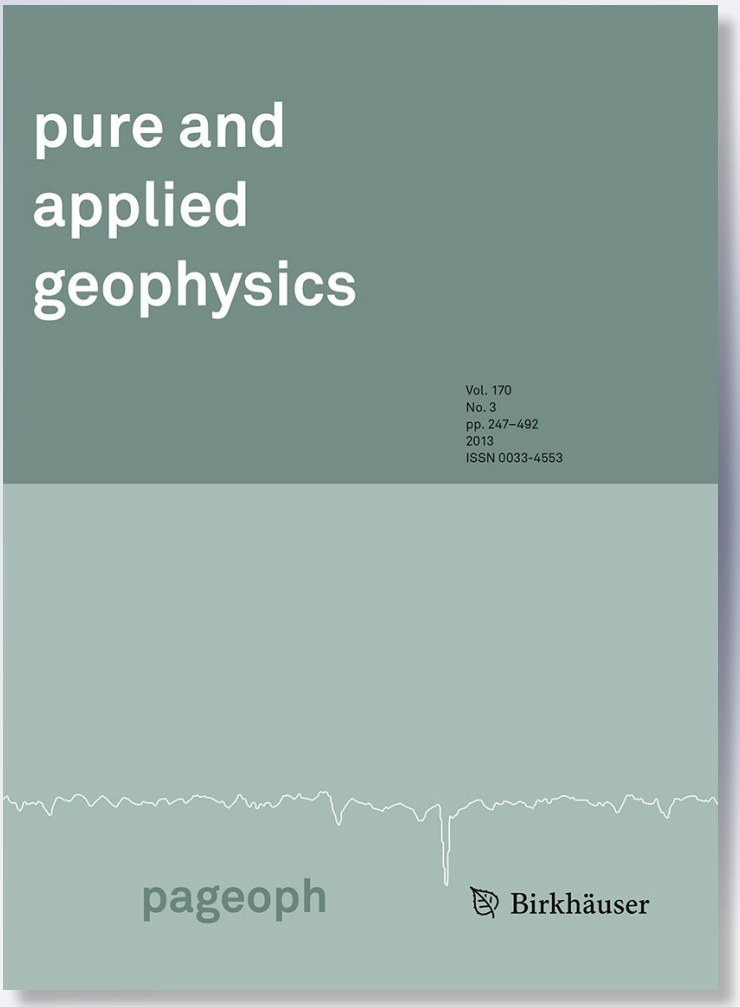

Springer

Pure Appl. Geophys. 170 (2013), 433–451

DOI 10.1007/s00024-012-0608-z

Pure and Applied Geophysics

Tsunami Modeling to Validate Slip Models of the 2007 M_w8.0 Pisco Earthquake, Central Peru

M. Ioualalen,[1] H. Perfettini,[2] S. Yauri Condo,[3] C. Jimenez,[4] and H. Tavera[3]

Abstract—Following the 2007, August 15th, M_w 8.0, Pisco earthquake in central Peru, Sladen *et al.* (J Geophys Res 115: B02405, 2010) have derived several slip models of this event. They inverted teleseismic data together with geodetic (InSAR) measurements to look for the co-seismic slip distribution on the fault plane, considering those data sets separately or jointly. But how close to the real slip distribution are those inverted slip models? To answer this crucial question, the authors generated some tsunami records based on their slip models and compared them to DART buoys, tsunami records, and available runup data. Such an approach requires a robust and accurate tsunami model (non-linear, dispersive, accurate bathymetry and topography, etc.) otherwise the differences between the data and the model may be attributed to the slip models themselves, though they arise from an incomplete tsunami simulation. The accuracy of a numerical tsunami simulation strongly depends, among others, on two important constraints: (i) A fine computational grid (and thus the bathymetry and topography data sets used) which is not always available, unfortunately, and (ii) a realistic tsunami propagation model including dispersion. Here, we extend Sladen's work using newly available data, namely a tide gauge record at Callao (Lima harbor) and the Chilean DART buoy record, while considering a complete set of runup data along with a more realistic tsunami numerical that accounts for dispersion, and also considering a fine-resolution computational grid, which is essential. Through these accurate numerical simulations we infer that the InSAR-based model is in better agreement with the tsunami data, studying the case of the Pisco earthquake indicating that geodetic data seems essential to recover the final co-seismic slip distribution on the rupture plane. Slip models based on teleseismic data are unable to describe the observed tsunami, suggesting that a significant amount of co-seismic slip may have been aseismic. Finally, we compute the runup distribution along the central part of the Peruvian coast to better understand the wave amplification/attenuation processes of the tsunami generated by the Pisco earthquake.

Key words: Tsunami, Pisco Peru, earthquake, inSAR, teleseismic.

[1] Géoazur, Université de Nice Sophia Antipolis, Institut de Recherche pour le Développement (IRD), Observatoire de la Côte d'Azur, 2 Quai de la Darse, BP 48, 06235 Villefranche-sur-mer Cedex, France. E-mail: Mansour.Ioualalen@geoazur.obs-vlfr.fr

[2] LGIT, Université Joseph Fourier, Institut de Recherche pour le Développement (IRD), Grenoble, France.

[3] Instituto Geofisico del Peru, Lima, Peru.

[4] Direccion de Hidrografia y Navegacion, DHN, Callao, Peru.

1. Introduction

Historically, the first slip models were based on seismological data. Near-field seismological data are not often available, and when they are, they require a good knowledge of the velocity structure of the area considered. Since those velocity models usually have a low spatial resolution (deca-kilometric in the best cases), they are unable to properly model the high-frequency content of seismograms. This is one of the reasons why teleseismic data are mostly used, since they involve distant stations for which high frequencies have been damped. They can give some hints about the dynamic of rupture, but suffer from a low spatial resolution due to their remote distance from the source.

Geodetic data, i.e., GPS (Global Position System) and Interferometric Synthetic Aperture Radar (InSAR), are interesting because they can detect slow deformation and are usually used in the near field. When applied to the study of the co-seismic phase, InSAR (Interferometric Synthetic Aperture Radar) data suffer from a lack of temporal resolution since they mostly consider a single measurement (the images being often separated by months), so that a significant amount of post-seismic slip may be included. However, the spatial resolution of InSAR has no equivalent, a pixel being of deca-metric size. GPS measurements, when operating continuously, have a good temporal resolution, up to 10 Hz of sampling rate, but they rely on the spatial density of the network, but are usually spatially scarce.

The fact that teleseismic and geodetic data are complementary, in terms of spatial and temporal resolution, explains why they are usually combined to infer the slip distribution on a fault. Doing so, we expect the derived slip model to be more robust than slip models obtained considering those data sets individually. The common view is that slip models

derived by combining various sets of data are more reliable than those considering single sets of data, simply because they should be more constrained.

We are concerned about the M_w8.0 earthquake/tsunami of Pisco of August 15th, 2007 in Central Peru (Fig. 1). Sladen *et al.* (2010) constructed three slip models that were obtained by inverting InSAR data only, teleseismic records only, and their combination. The authors extensively discuss the slip information obtained from those three inversions. As usual in a multi-data processing, it is difficult to estimate the respective limitations and information of every set of data. All depend on the data relevance themselves, their processing, the specific case study (location of the earthquake epicenter with respect to the records), the characteristics of the records (static vs. dynamic records), the spatio-temporal distribution of the records, the velocity model, and so forth. In this context, it is relevant to consider a further independent source of information to cross-validate the slip models.

The Pisco earthquake being tsunamigenic, it is natural to compare those slip models to the hydrographic records. The data considered by Sladen *et al.* (2010) were composed of DART buoys tsunami records and sparse available runup data. Despite their remarkable inversion processing and coherent slip distribution analysis, validation through these tsunami records was not quite conclusive, certainly because this effort would require an independent study by itself and was therefore beyond the scope of their work. The reasons for this discrepancy are that offshore DART buoys are generally convenient because the tsunami computations do not require reproduction of the full physics of the wave propagation, such as bottom friction, non-linearity, wave breaking parameterization, or coastline treatment. This latter issue is indeed an advantage for DART buoys because there is no need to construct a priori an accurate computational domain. (Sladen *et al.*, 2010 used a very scarce 2 min ETOPO-2 bathymetry). Another problem is that the authors have used a non-dispersive, non-linear shallow water model, so one may wonders whether the lack of dispersion is problematic or not. This is an issue that we propose to test in the present paper. Another issue concerns slip model validation with the runup observations. Sladen *et al.* (2010) have constructed a coastal area with ETOPO-2 bathymetry and topography. They did their validation by comparing two distinct features, i.e., the observed runup and the simulated wave heights (not runup) in the neighborhood of the coast at the 2 and 50 m isobaths. Obviously, the use of ETOPO-2 and a scarce grid is not relevant because the local slope effect, bathymetric shape uncertainty, and the lack of accurate topography may eventually lead to errors that can be larger in magnitude than the observed runup themselves. Finally, their validation of both DART buoys and runup observations were not conclusive: the nearest DART buoy that they processed is located 800 km south of the rupture (buoy 32401, located offshore of Chile) and the others are located thousands of kilometers offshore on the open Pacific ocean. At the Chilean station, the wave oscillates in the approximate range -1.5 to $+3$ cm. Whatever slip model they considered, their simulated waves under-predict observations by a factor of approximately 2/3, raising the question of whether the first wave is a peak or a trough. At this stage, the authors were unable to state whether or not the under-prediction was due to the uncertainty of their simulation (e.g., use of ETOPO-2 only, lack of dispersion, etc.) or to an inappropriate slip model. Additionally, for further sites, the questioning of the parameterization of viscous damping is also legitimate. For the runup observations, over-predictions and under-predictions are equally distributed (objective statistics are missing in their analysis). Here again, the differences cannot be explained objectively, and it is difficult to know if the observed discrepancies are due to the slip model used to compute the initial sea floor displacements. The goal of our study is to identify the slip model in better agreement with the tsunami data.

We propose to validate Sladen's slip models considering a realistic dispersive tsunami model with an accurate bathymetry and new runup data. To do so, we will use a dispersive fully nonlinear Boussinesq model (*Funwave*) with an accurate bathymetric data set (digitized high resolution marine charts) along with SRTM land topography of 90 m spatial resolution. Like Sladen *et al.* (2010) we process the Chilean DART buoy and further test dispersive effects, but we also enriched the tsunami data available by a full set of runup observations and a tide gauge record at Callao, Lima harbor. Tide

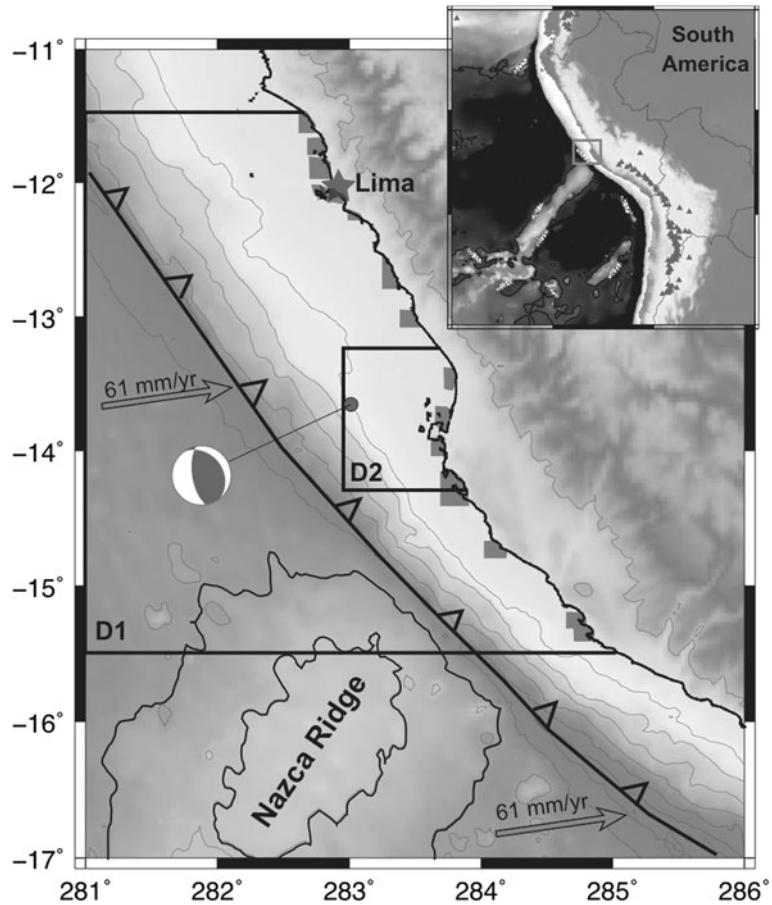

Figure 1
Computational domains D1 and D2 (300 and 50 m of grid spacing and 0.4 and 0.1 s of time step respectively) for the tsunami propagation/runup simulation. The *circle* represents the Pisco earthquake epicenter together with the CMT solution, while the *star* is for the Callao tide gauge location (locate in the harbor of the city of Lima). The background bathymetry is represented with 1,000 m iso-contours. The *grey rectangles* represent DHN high-density bathymetric survey

gauge processing is always challenging because recovery of the signal requires an extremely well-built simulation of the propagation and the coastal signature of the tsunami. The DART buoys are off-shore, and the simulated tsunami will propagate within a computational grid composed of 2′ ETOPO-2 data only. The 2′ spatial resolution of ETOPO-2 is not really questionable because typically, for a water depth of 4,000 m, it takes only about 10 s for the wave to propagate from one grid point to another, a value much smaller than the tsunami wave period itself. Still, the uncertainty of ETOPO-2 bathymetric data themselves is always questionable (although useful indeed) when only this data set is considered without a comparison with other more precise bathymetric data derived, for instance, from marine charts or multi-beams.

Finally, we will build considering our best-fit model a runup map all along the Central coast of Peru in order to identify the processes responsible for the local wave amplification/attenuation of the wave. Such a result has implications in terms of tsunami hazards.

2. The Geological and Seismological Constraints of Central Peru

2.1. The Geodynamical Context

Geodynamics in Peru is dominated by the convergence between the Nazca and the South American

plates with a relative velocity of about 67 mm/year orientated N78°E (DeMets *et al.*, 1990; Kendrick *et al.*, 2001) (Fig. 1). Within this context, Peru has been strongly affected by the occurrence of large interplate and intraplate earthquakes along its territory. More specifically, the central region of Peru has been affected by major tsunamigenic earthquakes showing irregular behavior in space and time such as the large earthquakes of 1604, 1664, 1687, 1746, 1868, including south of the Nazca ridge, the 1942 (M_w8.1), the 1996 (M_w7.7) and the 2001 (M_w8.4) events, and north of the ridge, the 1940 (M_w7.8) and 1974 (M_w7.9) earthquakes (Dorbath *et al.*, 1990; Beck and Ruff, 1989; Beck and Nishenko, 1990). Previous studies have identified a seismic gap between the 1974 event and the 1942 and 1996 ones that had not yet experienced a large earthquake since 1746 (Kelleher, 1972; Beck and Nishenko, 1990; Dorbath *et al.*, 1990; Swenson and Beck, 1996, 1999). Finally, on August 15, 2007 the Pisco earthquake struck within this gap, releasing the accumulated the strain accumulated during the last 261 years (the last event in this area being the 1746 event).

The Nazca ridge stands on the southern edge of the Pisco rupture. This very large heterogeneity, elevated more than 2 km above the oceanic floor with a width of about 200 km, has a great influence on the geodynamics of Peru. First of all, where it subducts the distance between the trench and the coast is the smallest along all the Peruvian margin. Second, no historical earthquake has struck in this area, although some significant events such as the 2007 earthquake or the 1996 Nazca earthquake have happened, respectively north and south of the ridge. Third, the seismic coupling, as inferred from campaign GPS measurements, is very low there, suggesting that this ridge could be an aseismic structure (Perfettini *et al.*, 2010). Those elements are consistent with the fact that the rupture of the Pisco earthquake stopped as it reached the ridge, and that most of the post-seismic slip was located on top of this structure (Perfettini *et al.*, 2010).

The Nazca ridge first reached the continent between 10 and 15 Myr ago, approximately at the level of the city of Trujillo (8°S), and drifted to the south to its present position (Gutscher *et al.*, 1999). During this drift, it is very likely that the ridge, assuming it is a creeping structure as discussed earlier, has left some indentations on the continental plate, increasing the degree of heterogeneity of the seismogenic fault zone. This idea is consistent with the fact that the area north of the ridge shows more frequent earthquakes, but of lower magnitude than south of the ridge, where the events tend to be much larger (Dorbath *et al.*, 1990). As discussed in the next section, the slow rupture velocity inferred from the seismic data during the Pisco earthquake may reflect the presence of a creeping band separating the two main co-seismic asperities.

2.2. *The August 15, 2007 Pisco Earthquake*

On 15 August 2007 at 23:40:57 GMT (18:40:57 local time) a M_w8.0 magnitude earthquake occurred at approximately 60 km west of Pisco (13.35°S, 76.51°W), Central Peru, and initiated at a depth of 39 km (NEIC). This earthquake released the strain accumulated inside the previous identified seismic gap located between the 1974 and the Nazca ridge (Beck and Nishenko, 1990). This event was felt in all cities along the Peruvian coastline from Piura (Northern Peru) to Arequipa (Southern Peru) with maximum intensity of VII–VIII (MM) in Pisco, Chincha and Canete (Tavera and Bernal, 2008), producing great destructions in Lima, Ica and Huncavelica, resulting in 595 fatalities and 318 missing people.

The CMT solution assigned to this event corresponds to a reverse faulting with a strike angle of 324°, a dip of 27° and a rake of 64°, with a seismic moment of 1.11×10^{21} N.m, corresponding to M_w8.0. Sladen *et al.* (2010) derived some kinematic slip models considering teleseismic and InSAR data. Three slip models were considered taking into account teleseismic data only, InSAR data only, and a combination of the two. Those three models show the same pattern with two main asperities, the largest on the northern edge of the Nazca ridge with peak slip values of the order of 10 m. The first asperity is located near the epicenter and the other (larger) one is located at approximately 60 km to the south (offshore the Paracas peninsula). The time lag between the rupture of those two asperities is about 60 s and the

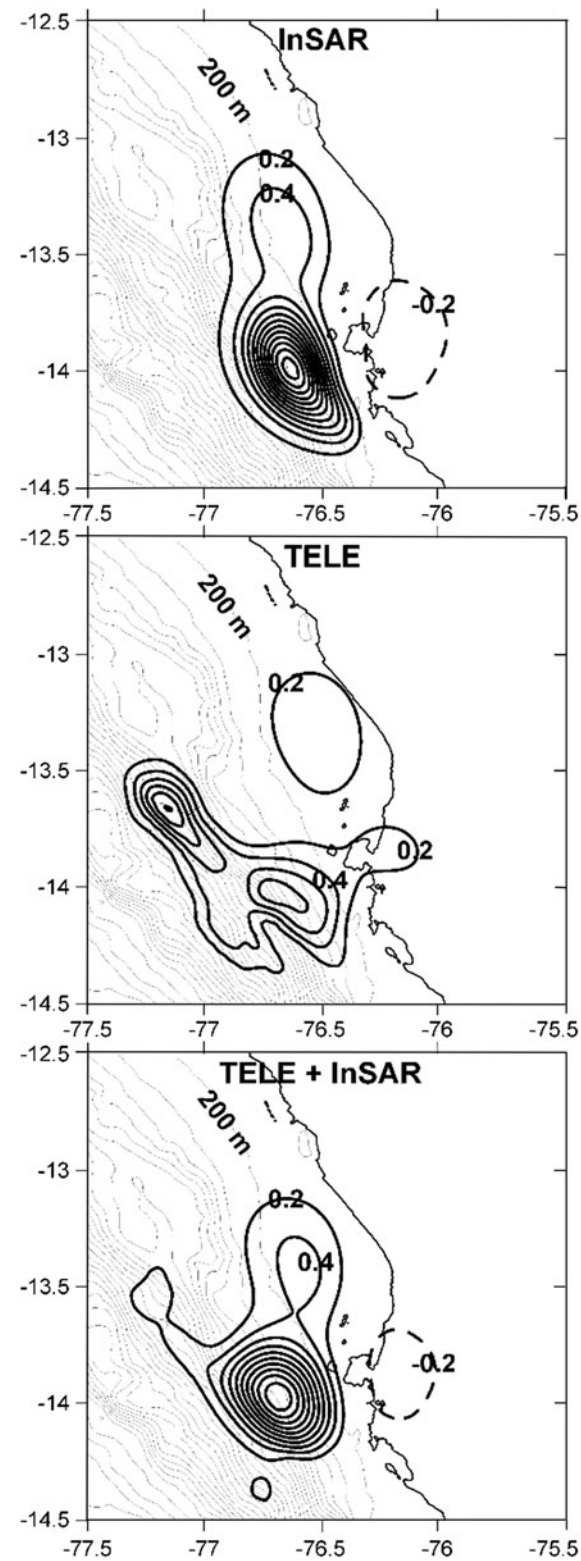

Figure 2
Seafloor vertical deformation (0.2 m iso-contours) for InSAR, teleseismic and their combination inversions (from Sladen*et al.*, 2010). The background bathymetry is represented with 200 m iso-contours

rupture velocity is less than 1.5 km/s. Obviously, this second patch is likely to have generated the high tsunami wave observed to the south of the Paracas peninsula. There, a 10 m runup was registered along with a 2–4 km inundation (Ronald Woodman, personal communication).

The InSAR interferogram is quite simple and could be adjusted with a single asperity as did in previous studies (Biggs *et al.*, 2009). But the existence of two asperities is consistent with the source time function that shows two distinct peaks, separated by 60 s of seismic quiescence (Sladen *et al.*, 2010). It is therefore required by the teleseismic data. An important issue discussed in Sladen *et al.* (2010) and Perfettini *et al.* (2010) is to know whether rupture really stops during this time lag, or continued aseismically.

2.3. Initial Sea Floor Displacement

In order to calculate the final co-seismic vertical displacements, we computed the vertical displacement induced by the slip models of Sladen *et al.* (2010) (Fig. 2). The vertical displacement field serves as an input to the tsunami propagation model (the initial wave). To do so, we calculate the Green functions using Okada's (1992) solution for surface displacement on a set of rectangular dislocations within an elastic half-space. A shear modulus of 5×10^{10} Pa was assumed.

3. Tsunami Observations

Fifteen to 20 min after the earthquake, the central coastline of Peru was swept by a tsunami that destroyed the village of Lagunillas, located 43 km south of the epicenter (south of the Paracas peninsula, Fig. 3). There, three people were killed after a succession of three to four significant waves. The highest observed wave rose by more than 2.5 m above the

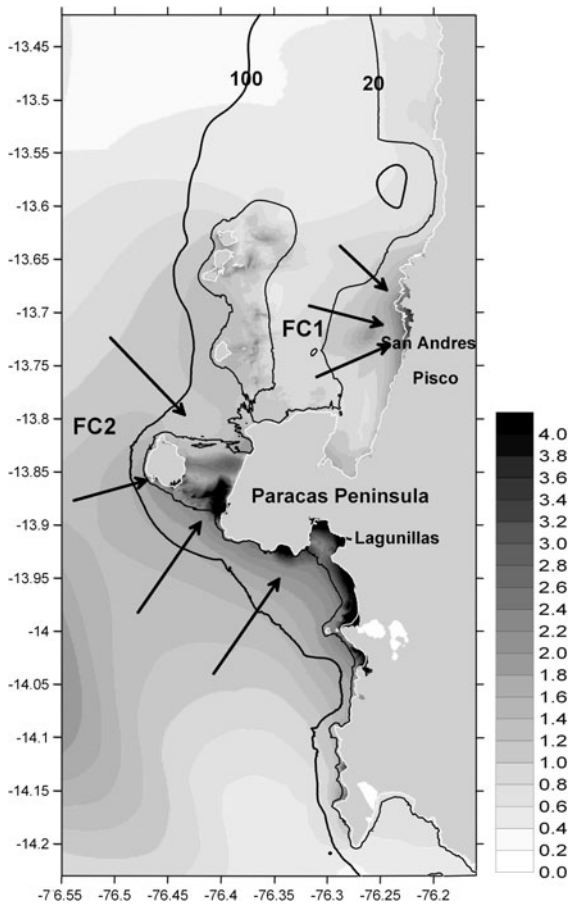

Figure 3
Simulated runup distribution using InSAR. The *color scale* has been limited to 4 (same color for runup >4 m). *FC1* and *FC2* indicate focusing areas. The 20 and 100 m isobaths are located. The initial coast line (before tsunami inundation) is plotted in *white* to locate the inundated zones

former high-tide position, flooding part of the village with more than 5 m of water. The wave reached 10 m at Yumaque (immediately south of Lagunillas). In other locations where the tsunami was reported moderate, it damaged fishing villages such as San Andres and El Chaco (immediately south of San Andres). At Lagunillas, waves lifted a ship from its moorings and carried it 1,500 m inland. The northern coastline of Paracas peninsula was locally inundated, flooding several houses. The highest observed wave there rose of only about 0.8 m above the former high-tide position. Residents reported that the sea withdrew immediately after the earthquake, just as it did at Lagunillas, before the arrival of the first wave. The wave activity was also observed in Callao harbor (180 km to north) past the night. Besides central Peru, the waves were registered almost all over the Pacific Ocean coasts, reaching Chile, California, New Zeland, Mexico, Hawaii and Japan with height of order of centimeters, e.g., 20 cm in Hokaiddo and 40 cm en Hilo.

Since the purpose of our study is to tentatively validate the earthquake source parameters of this event through the tsunami information, we need an objective set of data. In particular, tsunami time series observations are ideal candidates because we may use robust criteria to cross-validate the tsunami and the earthquake parameters, e.g, the wave period, arrival time, crest/trough amplitudes and wave sequence. Tide gauge records are essential in that context although very challenging to process. The nearest one from the epicenter is located in Pisco (approx. 33 km from the epicenter), but unfortunately it has been destroyed by the tsunami impact. Fortunately, another tide gauge record is available for this event at Callao (Lima harbor), approximately 180 km to the north (12°03′55″S; 77°09′52″W) (Fig. 1). The tide gauge is operated by the Direccion de Higrografia y Navegacion (DHN), which is responsible of the National Tsunami Warning System (SNAT). In addition, a significant amount of runup information is available for the event. Also, like did Sladen *et al.* (2010) the Chilean DART buoy 32401, located at approximately. 180 km to the north (19.297°S; 74.746°W), has also been processed and used for our validation purpose.

After the tsunami, many direct measurements of the generated tsunami were operated (Barrientos, 2007; Woodman, 2007; Ocola, 2007; DHN, 2007). We report in Table 1 the entire set of robust runup data. For the comparison between the observed and the simulated runup we took into account only the data for which the bathymetry has been well sampled (Fig. 1), i.e., the observations where the computational domain integrates only the ETOPO-2 data have not been considered for obvious accuracy reasons.

A low-pass Hanning filter has been processed to the Callao tide gauge record in order to isolate the tidal signal (a 1 h-cutting period). A further 5 min-period filtering has been applied to filter the high frequency swell (the tsunami period is approx. 20 min). The tide residual is obtained by subtracting the tide from the total signal (Fig. 4). The tide gauge clock is a recurrent issue:

Table 1

Observed (Obs.) and simulated runup for the two grid spacings 300 and 50 m (only around the Paracas peninsula) obtained with the InSAR, teleseismic (TELE) and their combination sources

Lat. (°S)	Long. (°W)	Obs. Runup (m)	InSAR		TELE	INSAR + TELE
			300 m	50 m	300 m	300 m
Barrientos (2007)						
12.287	76.881	1.18	1.02		0.78	0.99
12.632	76.821	0.87	0.62		0.63	0.72
13.028	76.486	0.75	1.76		1.41	1.54
13.729	76.223	2.65	2.48	2.88	1.22	2.20
DHN (2007)						
12.246	76.943	2.14	0.83		0.68	0.83
13.027	76.483	1.92	2.19		1.49	2.18
13.020	76.482	1.95	1.80		1.38	1.74
13.448	76.188	1.73	1.48	1.57	1.70	1.30
13.698	76.221	3.33	3.46	4.00	2.06	2.29
13.710	76.218	2.32	3.06	3.09	1.60	2.55
13.718	76.222	2.62	3.49	3.27	1.67	2.93
13.727	76.223	2.69	2.48	2.80	1.39	2.17
13.736	76.226	2.25	2.19	2.63	1.00	2.01
13.745	76.228	2.32	2.38	2.19	1.11	2.14
13.893	76.314	5.60	2.18	5.31	0.83	1.60
13.908	76.284	10.00	2.46	10.44	0.65	2.35
13.911	76.282	7.00	2.96	6.62	0.70	2.67
Woodman (2007)						
12.610	76.688	1.84	0.54		0.64	0.65
13.911	76.277	4.39	2.96	5.36	0.70	2.35
13.917	76.281	8.84	3.54	6.30	0.75	2.57
14.022	76.270	3.84	2.50	4.84	0.70	1.66
Ocola (2007)						
13.897	76.312	5.20	3.77	5.02	0.83	2.58
14.252	76.128	1.20	1.23	0.96	0.41	1.27
14.371	76.092	1.10	0.74		0.39	0.92

Note that only recorded runup where DHN bathymetry is available have been selected. Available records at regions of matching between DHN and ETOPO-2 data have not been selected as well for obvious possible incoherency between the two data sets at their respective limits

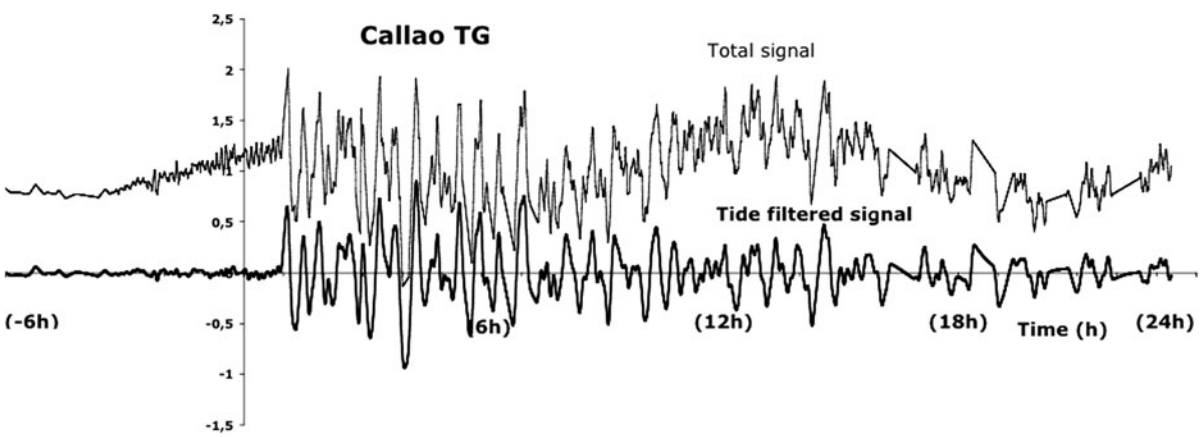

Figure 4

Wave height for the digitalized Callao tide gauge (TG) record (*upper graph*, in m) (see Fig. 1 for the TG location). A 1 h-period low-pass Hanning filter is applied to derive the tide-filtered signal (*lower bolded graph*). Time $t = 0$ corresponds to the earthquake occurrence (15th August 2007, 23:40:57 GMT, 18:40:57 local time)

tide gauges records are often subject to significant errors, even though we do not know if that is the case here. We prefer, however, to raise the issue and tentatively resolve it. It is then impossible to use the tsunami arrival time as a criterion in the source validation process. Unfortunately, this is the case for Callao. As a consequence, we will fit the time sequences of the recorded and simulated signals by finding their best cross-correlation as discussed later.

4. The Tsunami Simulation

4.1. The Computational Domain

In this study we use a parallelized version of *Funwave*, a fully nonlinear and dispersive model to compute the tsunami propagation and the runup/inundation (Wei *et al.*, 1995; Pophet *et al.*, 2010). For the Callao tide gauge simulations, we have built a $dx = dy = 300$ m grid-spacing computational domain ranging from 15.5 to 11.5°S and from 79 to 75°W (1,082 × 1,480 grid nodes). An empirical optimum time step of $dt = 0.4$ s was chosen with the relation $dt = 0.3\ \min(dx,dy)/\sqrt{gh_{\max}}$. This relation is the so-called CFL criterion (CFL for *Courant–Friedrichs–Lewy*), where g is for gravity, $h_{\max}$ is the maximum water depth of the computational domain (here 6,117 m) and dx and dy are the grid spacing, i.e., 300 m. A 3-h propagation time has been chosen in order to simulate a significant amount of waves for comparison with the Callao tide gauge record (27,000 time steps).

As far as the computational domain is concerned, three sets of data were used: The bathymetric data at specific areas were obtained from digitalized marine charts operated by the Peruvian Navy Direccion de Hidrografia y Navegacion (DHN) (Fig. 1). Elsewhere, ETOPO-2 data have been used to complement the bathymetry field. The inland topography was derived from the USGS Shuttle Radar Topography Mission (SRTM) (90 m of spatial resolution). In the present work, we will compare the predictions of the model to the data only in areas where we have a good matching between topography and bathymetry, i.e., at the junction between SRTM and DHN data (and not at the ETOPO-2 and SRTM data).

4.2. The Numerical Results for the Callao Tide Gauge

The comparison between the recorded and simulated tide gauge is performed from the arrival time (defined here as the time when the first wave is detectable/noticeable). It is found to be 3350 s (Fig. 4). Since we cannot use the arrival time of the tsunami, we chose to find a best-fitted time shift of the simulated tide gauge. This specific time shift will be set by finding the best cross-correlation between the simulated and the recorded tide gauge for the 2 first periods, i.e., approx 45 min of propagation. The best-fitted shifts for the simulated tide gauge are (−80, −40, −80) s for the InSAR, the teleseismic and the combination of the two data sets, respectively. Bearing in mind the slight imprecision of the offshore bathymetry, such lagging values are indeed negligible, supporting a satisfactory localization of the rupture for teleseismic and InSAR solutions. Thus, the tide gauge clock looks correct, and this problem is considered solved. Then the statistics will be performed for various time windows (30, 60 and 90 min) to test the statistics over the propagation time. The respective wave spectrum will also be computed. The best scenario will be selected based on the highest cross-correlation *corr* and determination coefficients R^2, the lowest norm L^2, the RMSE (the square root of the variance, a frequently used measure of the differences between values predicted by a model and the values observed) as well as the nearest *mean* and standard deviation STD.

Using the InSAR source model, the tide gauge record and the simulated one are in very good agreement, especially for the first three crests and troughs (Fig. 5). This is confirmed by the statistics that appear excellent for this source until 60 min after the tsunami arrival time at the Callao tide gauge, i.e., up to approximately 7100 s of total simulated tsunami propagation time in Fig. 4 (Table 2). For the 60-min window, the statistics show that the wave period and amplitude are very well-simulated, with a cross-correlation coefficient $Corr = 0.82$ close to unity (even more satisfactory with 0.94 for the 30 min of comparison) and a standard deviation STD difference of +1 % only. For the first 5,120 s time window, the wave spectra of the recorded and

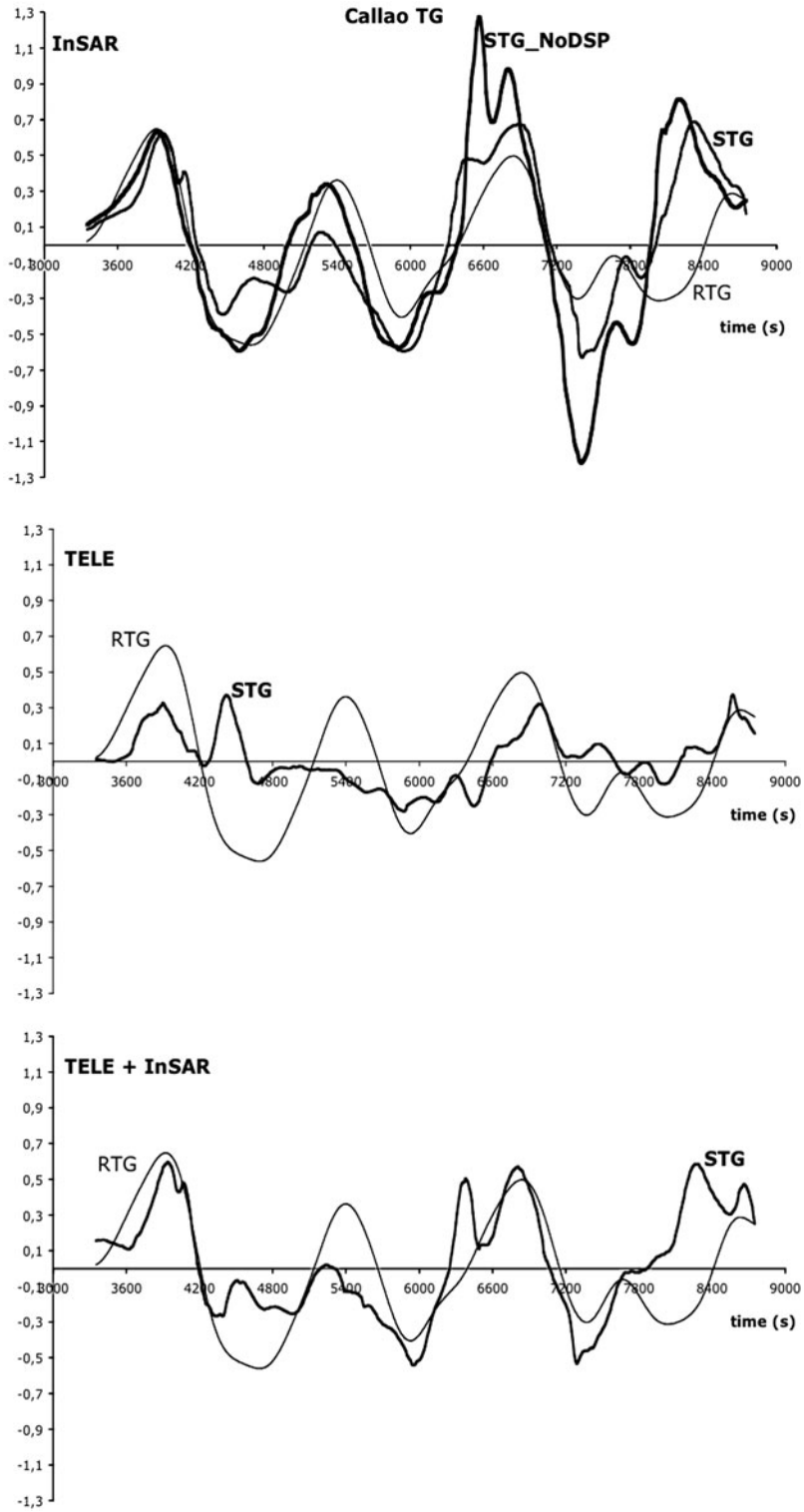

Figure 5
The recorded (RTG) and simulated (*bolded STG*) tide gauge of Callao for InSAR, teleseismic (TELE) and their combination. For InSAR, STG-NoDSP (*over-bolded black*) corresponds to a simulation without dispersion (nonlinear shallow water simulation)

Table 2

Comparison between recorded (RTG) and simulated (STG) tide gauges for InSAR, teleseismic (TELE) and their combination along with InSAR for a non-dispersive configuration (InSAR-NoDSP) at Callao for different time windows (30, 60 and 90 min)

Time windows for comparison between RTG and STG at Callao												
	30 min				60 min				90 min				
	RTG	InSAR	TELE	INSAR + TELE	RTG	InSAR	TELE	INSAR + TELE	RTG	InSAR	TS	INSAR + TELE	InSAR-NODSP
Mean (m)	–0.025	0.036	0.076	0.038	0.026	0.021	–0.011	0.017	–0.08	0.040	0.016	0.036	0.017
STD (m)	0.417	0.301	0.137	0.264	0.362	0.366	0.163	0.299	0.324	0.376	0.155	0.306	0.521
RMSE (m)		0.180	0.389	0.216		0.221	0.332	0.231		0.283	0.293	0.272	0.386
R^2		0.813	0.132	0.733		0.628	0.160	0.591		0.234	0.177	0.293	–0.425
L^2		0.431	0.930	0.516		0.608	0.914	0.637		0.874	0.907	0.840	1.193
Corr.		0.939	0.453	0.913		0.817	0.414	0.772		0.692	0.430	0.637	0.675

The basic statistics are the mean wave height *Mean*, the standard deviation *STD*, the root mean squared error *RMSE*, the determination coefficient R^2, the norm L^2 and the cross-correlation coefficient *Corr*. The usual RMSE representing the model skill is defined as $\mathrm{RMSE} = \sqrt{\sum_i (\eta_{RTGi} - \eta_{STGi})^2 / n}$, where η_{RTGi} corresponds to a tide gauge record point, η_{STGi} is for the associated simulated one and n is the number of comparison points (every 10 s). The determination coefficient R^2 is defined as $R^2 = 1 - \sum_i (\eta_{RTGi} - \eta_{STGi})^2 \Big/ \sum_i (\eta_{RTGi} - \mathrm{Mean})^2$. The Norm L^2 is defined as $L^2 = \sum_i (\eta_{RTGi} - \eta_{STGi})^2 \Big/ \sum_i \eta_{RTGi}^2$

simulated tide gauge are also much alike; their energy distribution is very similar, with two period peaks at 640 and 1,280 s of very similar amplitude (Fig. 6). The agreement between the model and the tide gauge data, both in the time and frequency domain, indicates that the sequence of waves, i.e., the relative amplitudes from one crest/trough to another (wave periods distribution, modulations, etc.), is well simulated by the InSAR source. At this stage it is fair to note that our grid spacing ($dx = dy = 300$ m) is quite large. However, the statistics are representative, very satisfactory and conclusive for the InSAR simulation. As a consequence, we may expect some slightly better validation by reducing the grid spacing, but not in a drastic way. Technically, the version of *Funwave* that has been used is parallelized (Popheт, *et al.*, 2010), but the grid spacing must be kept constant (uniform grid). Our limited computing facility (8 unit-cluster) does not allow us to simulate a large D1 domain with a 50 m uniform grid spacing because a single simulation would take several CPU weeks.

For the teleseismic source, the validation is not satisfactory for the times series (Fig. 5), the statistics (Table 2) and the period spectrum (Fig. 6). The wave phase and amplitude are poorly simulated. The cross-correlation coefficient is 0.45 for 30 min of comparison and a STD difference of –67 %. Their respective period energies differ significantly in amplitude and phase (569 and 640 s and 1,280 and 1,780 s, respectively) indicating a poor representation of the wave sequence unlike the InSAR model. The signal exhibits a higher frequency content compared to the InSAR solution because the initial waveform is more heterogeneous (rougher) (Fig. 2).

The combined slip model based on the combination of InSAR and teleseismic data should theoretically be the most realistic representation of the co-seismic deformation (which are the initial conditions for the tsunami model), simply because it considers the deformation due to both contributions and would be expected to be more constrained. Looking at Fig. 5 and Table 2, we can see that, although in better agreement with the data than the teleseismic model, the combined slip model does a worse job than the InSAR-only slip model. Clearly, the inclusion of teleseismic data is responsible for

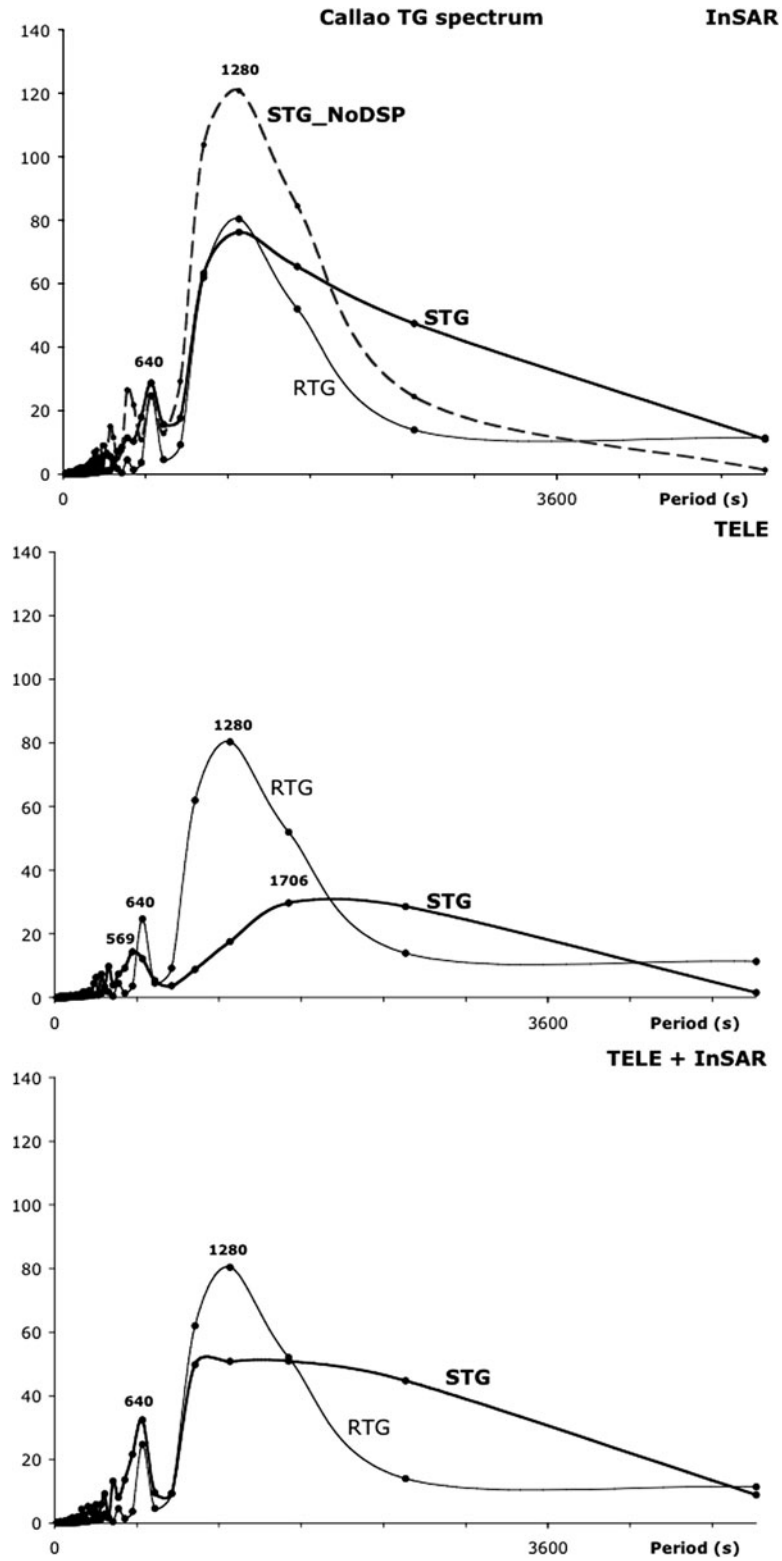

Figure 6
The computed period spectra for the recorded (RTG) and simulated (*bolded STG*) tide gauge of Callao for InSAR, teleseismic (TELE) and their combination. For InSAR, STG-NoDSP (*dashed*) corresponds to a simulation without dispersion (nonlinear shallow water simulation). A 5,120 s spectrum window has been taken (the period when a tsunami signal is detected at Callao tide gauge, i.e., total time of simulation minus the arrival time)

this disagreement. Looking at Fig. 2, it can be seen that the teleseismic data predict a co-seismic displacement field with two patches of significant displacements (located along the 60 s isochron as may be seen in Fig. 10 of SLADEN *et al.* (2010), while InSAR data mostly present a single area of high vertical displacement, on top of the main asperity of the Pisco rupture. The combined model deviates from the InSAR model because of the presence of this second slip patch, localized at approximately 77.2°W − 13.5°S (Fig. 2). This two-peak distribution is responsible for the higher-than-expected frequency content of the tsunami waves (Figs. 5, 6).

To further justify our study and compare our results with the tsunami validation of SLADEN *et al.* (2010), we performed a sensitivity test for the InSAR solution to examine the role of dispersion, a process that has not been considered in their simulation (Fig. 5). Dispersive effects are quite important in coastal areas, in particular for the delayed crests/troughs (after the first wave) when high frequency waves traveling slower than the leading wave train reach the site. The wave height may eventually double (e.g, the second crest/trough). As a result, it is hopeless to tentatively perform any kind of conclusive slip model validation without considering dispersion. The statistics displayed in Table 2 for InSAR indicate a clear difference in considering dispersive effects or not. The 'non-dispersive' wave spectrum indicates an over-dominant low-frequency mode (at 1,280 s in Fig. 6) and misrepresents the tsunami frequency re-distribution at coastal areas. Consequently, we absolutely recommend the consideration of dispersion near coastal areas.

4.3. The Chilean DART Buoy Record Validation

To validate the Chilean buoy record 32401, we have used the ETOPO-2 data set to construct the entire computational domain ranging from 20 to 12°S in latitude and from 80°W to 70°E in longitude with a 600 m grid spacing and an associated 0.6 s time step. This time, 4 h of tsunami propagation are simulated in order to reproduce the leading waves sequence.

As for the Callao tide gauge, a low-pass Hanning filter has been processed for the DART record (a 1-h cutting period) in order to isolate the tide (Fig. 7). We haven't been able to filter the oscillations clearly visible immediately after the earthquake occurrence (Fig. 7). These oscillations are seismic surface waves (SLADEN *et al.*, 2010), and unfortunately their range of frequencies includes that of the tsunami arriving approximately 50 min after the earthquake occurrence. A high-pass filtering is then prohibited. However, their amplitude is nearly damped at the tsunami arrival, avoiding any tsunami signal contamination.

We have found that the simulated tsunami signals at the DART Chilean buoy is absolutely not affected by dispersion (comparison not shown here since they are identical). GRILLI *et al.* (2007) and IOUALALEN *et al.* (2007) computed the dispersive effects of the 2004 Sumatra event: They showed how dispersive effects may be crucial mainly along the main tsunami wave directivity (across-faulting), then decaying aside. A simple explanation follows: aside of the wave directivity, the tsunami wavelength is generally larger, yielding a smaller kh, where k is the tsunami wavelength and h is the local water depth. Consequently the shallow water assumption $kh \to 0$ applies more strongly, and thus dispersive effects are minimized. Similarly, the Chilean DART buoy is located much (southward) aside of the nearly east–west tsunami directivity, and thus the tsunami propagation is not likely to be affected by dispersion. We expect that it should be different for the other DART buoys considered in SLADEN *et al.* (2010). Consequently the role of dispersion is difficult to anticipate, depending on the wave directivity, the water column elevation and local site effects. As a result, like GRILLI *et al.* (2007) and IOUALALEN *et al.* (2007), we recommend the use of a dispersive tsunami propagation model, especially for validation of slip models or inversion procedures. Not doing so would be risky, as one is unable to estimate properly the amount of tsunami signal (phase and amplitude) due to the source or to an inaccurate non-dispersive model. Nowadays this is

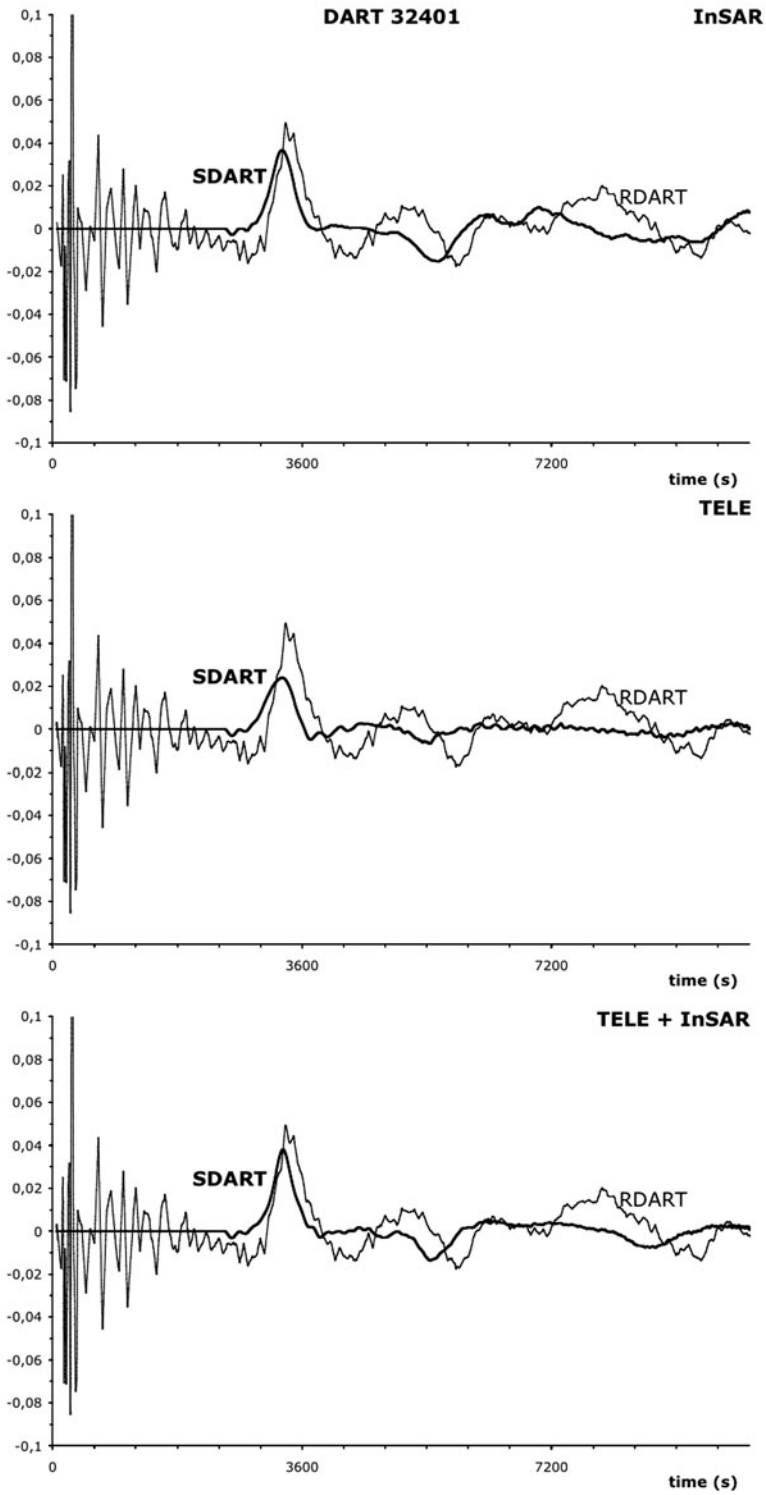

Figure 7
The recorded (RDART) and simulated (*bolded SDART*) signal of the Chilean 32401DART buoy for InSAR, teleseismic (TELE) and their combination. This time non-dispersive results (nonlinear shallow water simulation) are strictly identical to dispersive ones (Boussinesq simulation)

Table 3

DART buoy 32401 statistics for InSAR, teleseismic (TELE) and their combination for a time window of 120 min

	Observed	32401 DART statistics		
		InSAR	TELE	INSAR + TELE
Mean (m)	0.0028	0.0012 (−57 %)	0.0010 (−64 %)	0.0012 (−57 %)
STD (m)	0.0117	0.0089 (−24 %)	0.0054 (−54 %)	0.0078 (−33 %)
RMSE (m)		0.0110	0.0104	0.0097
R^2		0.21	0.22	0.31
L^2		0.86	0.86	0.81
Corr.		0.54	0.49	0.58

a crucial aspect, since DART buoys are very commonly used for these purposes.

When compared to the Chilean DART record, neither the simulated tsunami signals (Fig. 7) nor the comparison statistics (Table 3) allow a clear identification of the best rupture scenario. All three sets of statistics indicate a reasonable fit with the record, but no scenario clearly differentiates from the others. The same statement applies when comparing the respective wave spectra (Fig. 8). The only interesting matter is that the first peak amplitude is reasonably reproduced for InSAR as in Sladen *et al.* (2010). Then for all slip models the following wave sequence (amplitude and phase) is less satisfactory. We simply attribute the deterioration in the wave sequence to ETOPO-2 bathymetry and topography uncertainties: the delayed sequence is more affected by the tsunami propagating (slower) near coastal area. There, these uncertainties are more crucial for a proper tsunami modeling. Remote validation or co-seismic slip inversions considering DART buoys may look appealing because they don't require a small grid spacing. But their major drawbacks are that (i) an often inaccurate offshore bathymetry, combined with (ii) a poor knowledge of the spatial distribution of wave dispersion, limit its efficiency. The above validation with the Callao tide gauge is more conclusive thanks to an accurate computational domain and the use of a dispersive model (*Funwave*) in coastal areas.

4.4. The Tsunami Wave Runup Validation

Runup data are time-integrated and represent the highest inundate land points over the entire tsunami propagation time. In the case of the Pisco earthquake, runup has been documented by Barrientos (2007), Woodman, (2007), Ocola (2007), and in DHN, (2007) (see Table 1 for a data compilation and the predictions of the three slip models). They are particularly useful to estimate the spatial resolution of our tsunami model. Note that neither the runup data nor the tide gauge data have been used for this validation process: They represent independent data sets to the teleseismic and InSAR data used to build the earthquake slip models, and can therefore be used to cross-validate those slip models.

In order to avoid a random comparison, we will take into consideration only runup records where we have an accurate DHN bathymetric data set (Fig. 1). Besides, we will not take into consideration records in the areas where we consider a non-satisfactory matching between DHN data and scarce ETOPO-2 bathymetric data. It is also fair to note that areas of accurate DHN bathymetry may be also problematic if the wave first propagates along an inaccurate bathymetry (prior to its arrival at the accurate subdomain). Here, we will not discuss this issue and will simply consider that this feature is integrated in our runup validation process among other source of uncertainties such as the source accuracy, the discretization domain, etc. Besides, some contradictions between runup values provided by the different authors of Table 1 can be noticed. Consequently when two nearby observed runup (corresponding to the same grid node) are too different, we select the closer in space and value from our simulations. Concerning our spatial resolution (dx and dy) we will make a sensitivity test for three values: $dx = dy = 300$ m and 50 m (for the InSAR source

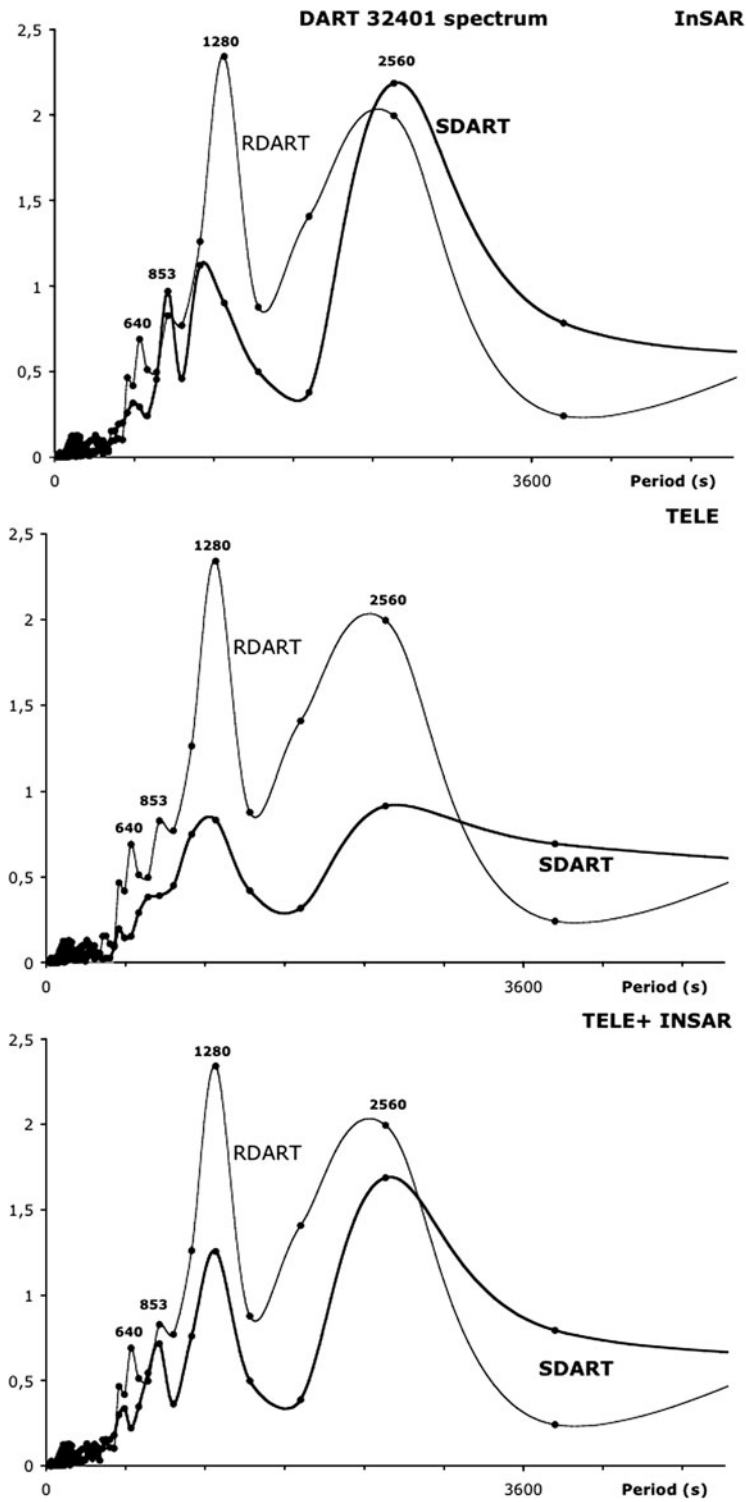

Figure 8
The computed period spectra for the recorded (RDART) and simulated (*bolded SDART*) of the Chilean 32401DART buoy for InSAR, teleseismic (TELE) and their combination. A 2-h spectrum window has been taken (the period when a tsunami signal is detected at the buoy, from 2,865 to 10,065 s after the earthquake occurence)

only). For the latter grid spacing, we have performed a further simulation within a restricted area (76.92°W–76.11°W; 14.3°S–13.32°S) in the vicinity of the Paracas Peninsula, which has been the most impacted area by the tsunami. The simulation covers a 1-h propagation time (36,000 time steps for a 0.1 s optimal time step).

As for Callao tide gauge comparison, our $dx = 300$ m simulation also indicates that the InSAR source model is the best candidate to reproduce the tsunami generated by the Pisco earthquake. For InSAR simulation, the cross-correlation is acceptable (0.58) but the STD is quite disappointing, i.e., a 60 % error (Table 4). The runup amplitude is clearly not reproduced. The main reason is the poor grid-spacing resolution. The much more accurate $dx = 50$ m simulation is excellent with a cross-correlation of 0.95 (to be compared with 0.39 for common data with 300 m resolution). The STD is only 2 % away from the observations. The RMSE, R^2 and L^2 are excellent (Table 4). The $dx = 50$ m simulation shows again how the construction of the computational grid and the use of a reliable bathymetric and topographic data sets is crucial. The excellent statistics of the runup comparison differ from those of Sladen *et al.* (2010) which are non-conclusive: Like for DART buoys, the runup simulations of Sladen *et al.* (2010) do not discriminate clearly between the slip models due to an incomplete tsunami model. To the contrary, our results based on a more realistic tsunami model demonstrate that the co-seismic slip model that better mimics the tsunami of the Pisco earthquake is the InSAR based slip model.

A full picture of the maxima of wave height is displayed in Fig. 3 for $dx = 50$ m grid spacing taking the InSAR solution (the overall best-candidate solution): The wave maxima appears in the vicinity of the area of maximum co-seismic slip (nearby the southern asperity), near Pisco and the Paracas Peninsula, which is the region of wave main directivity. However, the main wave amplification factor is focusing; the wave is first sharply refracted from the FC1 and FC2 areas hosting the convex-shaped 20 and 100 m isobaths, and then focuses (Fig. 3). Based on the excellent statistics of Table 3, we believe we have provided here a synoptic picture of the event in a prognostic mode since the runup observations have not been further used for the source calibration provided by Sladen *et al.* (2010).

5. Conclusion

Considering various slip models of the 2007 M_w8.0 Pisco earthquake built by Sladen *et al.* (2010) and based on teleseismic data, InSAR data, and their combination, we have designed robust tsunami simulations to compare/validate those slip models with an independent set of unpublished hydrographic data. Unfortunately, Sladen's *et al.* (2010) tsunami model has not been conclusive for various reasons depending on the choice of the hydrographic data they have considered and a rough bathymetry. We want to stress here that their main preoccupation was to build robust earthquake slip models and not to build a tsunami model, which is the main concern of our

Table 4

Runup statistics for InSAR, teleseismic (TS) and their combination (COMB)

	Observed	Runup statistics				
	300 m (50 m)	InSAR (300 m)	InSAR (300 m)_BIS	InSAR (50 m)	TS (300 m)	COMB (300 m)
Mean (m)	3.24 (4.12)	2.17 (−33 %)	2.66 (−35 %)	4.20 (+2 %)	1.03 (−68 %)	1.87 (−42 %)
STD (m)	2.41 (2.50)	0.96 (−60 %)	0.70 (−72 %)	2.27 (−9 %)	0.45 (−81 %)	0.67 (−72 %)
RMSE (m)		2.28	2.74	0.81	3.37	2.51
R^2		0.10	−0.20	0.89	−0.96	−0.09
L^2		0.57	0.57	0.17	0.84	0.62
Corr.		0.58	0.39	0.95	−0.23	0.56

Two simulations results are reported: They correspond to the grid spacings $dx = 300$ m (computational domain D1 in Fig. 1) and $dx = 50$ m (D2 in Fig. 1). The ensemble InSAR (300 m)_BIS applies for the sub-ensemble of data for 300 m that is common to the data of 50 m in Table 1

paper. Our more realistic approach allows models discrimination using hydrographical data. Among the three slip models they have proposed, we show clearly that the InSAR based slip model is the most satisfactory in terms of tsunami data. The hydrographic validation is a necessary requirement to fully assess the real earthquake slip characteristics. For all of their tsunami simulations, Sladen *et al.* (2010) have used a very scarce grid built with 2′ ETOPO-2 data which should not be a crucial issue for offshore DART records (as far as the bathymetric data are accurate which is not always the case), but it is of primary concern for runup data: (1) The first data set used were remote DART buoys tsunami records. DART data are interesting because they are not contaminated by local site effects; however, to what extent is ETOPO satisfactory even on deep water? (2) The second data set was an ensemble of observed runup data. Here again, their computational domain was too scarce to properly reproduce the observed runup distribution. *In fine*, their tsunami simulations were not conclusive, and the objective of the present study was to complement their study.

For that purpose, we have constructed a tsunami model using the three slip models of Sladen *et al.* (2010) to model the initial wave. We believe our simulations are robust because they are based on an accurate construction of the computational domain (fine bathymetry and topography) and on the use of a reliable wave propagation dispersive model, i.e., a *Funwave* fully nonlinear Boussinesq model. Like Grilli *et al.* (2007) and Ioualalen *et al.* (2007) we show how dispersive effects may be difficult to anticipate vs., wave directivity, the local bathymetry, and coastal configuration. In that context we suggest that crucial numerical procedures, like rupture inversion or validation with hydrographic data, require taking wave dispersion into account.

We compare the predictions of our modeling to a tide gauge record at Callao (Lima harbor). Then, like Sladen *et al.* (2010), we process a slip validation at the Chilean 32401 DART buoy, with, however, a further sensitivity test on dispersion effects. Finally, available non-published runup data near the epicentral are processed. Like DART records, the Callao tide gauge record is interesting because the time series allows a full validation that takes into account the wave behavior at this site, i.e., the time varying wave amplitude, the wave periodicity, and the wave sequence (alternation of peak and troughs and their relative amplitude). Runup data are time integrated, but they are also interesting because they are representative of the spatial distribution of the wave along the coast. Both sets of data were compared to our modeling results. Various statistical tools (respective mean, standard deviation, RMSE, Norm, determination and cross-correlation coefficients) were used, together with a spectral analysis of the tide gauge time series (a good indicator of the wave sequence), to estimate the degree of agreement between the data and the model.

The tide gauge record and the simulated ones are in very good agreement considering the InSAR-based slip model. The statistics show that the wave period and amplitude are very well simulated and that the wave spectra of the recorded and simulated tide gauge are similar with very close peaks of energy. To the contrary, the teleseismic simulation exhibits a poor agreement with the data, in particular, with weaker amplitudes and higher-than-expected frequency content. Consequently, the combination of InSAR and teleseismic data yields a deterioration of the InSAR simulation, but is better than the teleseismic-only slip model. The same conclusions apply for the runup comparison, which exhibit even more satisfactory statistics for the InSAR-based slip model. It is surprising that a model containing more data, and therefore more constraints, leads to physical predictions in worse agreement with the observation than a physical model incorporating less data. Conceptually, this is possible only if the data incorporated are biased, incomplete or inappropriate. As discussed earlier, we believe that in the particular example of the Pisco earthquake, this incompleteness may arise from the fact that, for this specific case study, teleseismic data may be possibly unable to detect aseismic slip, while geodetic (InSAR here) can.

This can be suggested using the following reasoning. The tidal gauge time series of Fig. 5 show a simple signal, with a dominant period. Since a period is dominating, the source of the signal implies, as a

first order approximation, a single wavelength, and hence a single displacement patch. As may be seen considering the teleseismic-based slip model, a two patches displacement distribution implies two wavelengths, appearing as secondary oscillations of Fig. 5. Therefore, and apart from any consideration about the slip model, the simplicity of the tide gauge time series implies an initial smooth displacement field, mostly characterized by a single patch. Noting that the source time function clearly exhibits two peaks (due to the 60 s of seismic quiescence), the tsunami observations suggest that co-seismic slip must have been more continuous than suggested by seismological data. The only way for this to be is to assume that a significant portion of aseismic slip happened in between the main co-seismic asperities. We suggest that this amount could possibly be of the order of 2 m on the fault plane itself.

Finally, we also simulated the runup distribution in Central Peru in a prognostic mode at a synoptic space scale for the event. In particular, a mapping of the wave amplification/attenuation processes has been proposed. As expected, refraction/focusing (wave convergence due to convex-shaped isobaths) has been found to be the main factor of wave amplification.

Acknowledgments

The authors are grateful to A. Sladen for providing the earthquake slip models used in this study and J.-P. Avouac, G. Hérail, M. Chlieh, B. Guillier and J.-X. Dessa for useful discussions. We wish to acknowledge two anonymous reviewers who, through their suggestions, have contributed to a substantial improvement of the first draft manuscript.

References

Barrientos, S. E. (2007) Informe sobre las alturas de “run-up” alcanzadas por el tsunami asociado al sismo $M_w = 8.0$ del 15 de Agosto de 2007 en la zona de Pisco. Peru, www.ceresis.org.

Beck, S., and Nishenko, S. (1990) *Variations in the mode of great earthquake rupture along the central Peru subduction zone*. Geophys. Res. Lett., *17*, 1969–1972.

Beck, S., and Ruff, L. (1989) *Great earthquake and subduction along the Peru trench*. Physics of The Earth and Planetary Interiors, *57*(3–4), 199–224.

Biggs, J., Robinson, D. P., and Dixon, T. H. (2009) *The 2007 Pisco, Peru, earthquake (M8.0): Seismology and geodesy*. Geophys. J. Int., *176*(3), 657–669, doi:10.1111/j.1365-246X.2008.03990.x.

DeMets, G., Gordon, R. G., Argus, D. F., and Stein, S. (1990) *Current plate motions*. Geophys. J. Int., *101*(2), 425–478.

DHN (2007) Informe post tsunami, http://www.dhn.mil.pe/docs/tsunami/Informe_Post_Tsunami_Pisco\%202007.pdf.

Dorbath, L., Cisternas, A., and Dorbath, C. (1990) *Assessment of the size of large and great historical earthquakes in Peru*. Bull. Seism. Soc. Am., *80*, 551–576.

Grilli, S. T., Ioualalen, M., Asavanant, J., Shi, F., Kirby, J. T., and Watts, P. (2007) *Source Constraints and Model Simulation of the December 26, 2004, Indian Ocean Tsunami*. J. Waterway, Port, Coastal and Ocean Eng., ASCE. doi:10.1061/(ASCE)0733-950X(2007)133:6(414).

Gutscher, M. A., Malavieille, J., Lallemand, S., and Collot, J.-Y. (1999) *Tectonic segmentation of the North Andean margin: impact of the Carnegie Ridge collision*. Earth and Planetary Science Letter, *168*, 255–270.

Ioualalen, M., Asavanant, J., Kaewbanjak, N., Grilli, S T., Kirby, J. T., and Watts, P. (2007) *Modeling the 26 December 2004 Indian Ocean tsunami: Case study of impact in Thailand*. J. Geophys. Res., *112*, C07024. doi:10.1029/2006JC003850.

Kelleher, J. (1972) *Rupture zones of large South American earthquakes and some predictions*. J. Geophys. Res., *77*, 2087–2103.

Kendrick, E., Bevis, M., Smalley, R. J., and Brooks, B. (2001) *An integrated crustal velocity field for the central Andes*. Geochemistry, Geophysics, Geosystems, *2*, doi:10.1029/2001GC000208.

Ocola, L. (2007) Aspectos fÌsicos del maremoto de Pisco del 15 de agosto 2007 y las inundaciones máximas. *In terremoto de Pisco (Peru) del 15 de Agosto de 2007 (8.0 Mw)*, edited by H. Tavera, Direccion de Sismologia en CNDG/Instituto Geofisico del Peru, 395–420.

Okada, S. (1992) *Internal deformation due to shear and tensile faults in a halfspace*. Bull. Seismol. Soc. Am., *82*, 1018–1040.

Perfettini, H., Avouac, J.-P., Tavera, H., Kositsky, A., Nocquet, J.-M., Bondoux, F., Chlieh, M., Sladen, A., Audin, L., Farber, D. L., and Soler, P. (2010) *Seismic and aseismic slip on the Central Peru megathrust*. Nature, *465*(7294), 78–81.

Pophet, N., Kaewbanjak, N., Asavanant, J., and Ioualalen, M. (2010) *High Grid Resolution and Parallelized Tsunami Simulation with Fully Nonlinear Boussinesq Equations*. Computers and Fluids, doi:10.1016/j.compfluid.2010.09.030.

Sladen, A., Tavera, H., Simons, M., Avouac, J.-P., Konca, A.O., Perfettini, H., Audin, L., Fielding, E. J., Ortega, F., and Cavagnoud, R. (2010) *Source model of the 2007 Mw8.0 Pisco, Peru earthquake: Implications for seismogenic behavior of subduction megathrusts*. J. Geophys. Res., *115*, B02405, doi:10.1029/2009JB006429.

Swenson, J., and Beck, S. (1996) *Historical 1942 Ecuador and 1942 Peru subduction Earthquakes, and Earthquakes cycles along Colombia-Ecuador and Peru Subduction Segments*. Pure and Applied Geophys., *146*, 67–101.

Swenson, J., and Beck, S. (1999) *Source characteristics of the November 12 1996 Mw = 7.7 Peru subduction zone earthquake*. Pure and Applied Geophys., *146*, 67–101.

Tavera, H., and Bernal, I. (2008) *The Pisco (Peru) earthquake of 15 August 2007*. Seismol. Res. Lett., *79*(4), 510–515, doi:10.1785/gssrl.79.4.510.

Wei, G., Kirby, J. T., Grilli, S. T., and Subramanya, R. (1995) *A fully nonlinear Boussinesq model for free surface waves. Part 1: Highly nonlinear unsteady waves*. J. Fluid Mech., *294*, 71–92.

Woodman, R. (2007) Observaciones del tsunami asociado con el terremoto de Pisco del 15 de Agosto 2007, In *El terremoto de Pisco (Peru) del 15 de Agosto de 2007 (8.0 Mw)}*, edited by H. Tavera, Direccion de Sismologia en CNDG/Instituto Geofisico del Peru, 351–362.

(Received February 3, 2012, revised April 29, 2012, accepted May 3, 2012, Published online October 5, 2012)